SAND--89-2967C

DE90 006277



# EXTERNAL MICRO ION-BEAM ANALYSIS (X-MIBA)*

B. L. Doyle, D. S. Walsh+ and S. R. Lee

Sandia National Laboratories, Albuquerque, NM 87185-5800
+Idaho State University, Pocatello, ID, 83209

ABSTRACT:

In-air or external ion beam analysis combined with 10-100 $\mu$m spatial resolution, is a truly unique feature of the nuclear microprobe technique. PIXE has been performed externally for many years, but recently, other IBA techniques such as backscattering and nuclear reaction depth profiling measurements have been made in air. Presently, the use of eXternal Micro Ion-Beam Analysis, or X-MIBA, is being attempted at a growing number of microprobe facilities; however, the full potential of this new technique remains relatively unexploited. This paper will review the X-MIBA technique with emphasis on 1) optimization of exit foil geometries, 2) beam focusing and spot size considerations, 3) external IBA techniques, and 4) radiation hazards associated with the direct and scattered beam, nuclear reaction products and radionuclei production in the air. The unique in-air analysis advantages of no pump down, and essentially unrestricted sample size or state (solid, liquid etc.), has resulted in a myriad of applications of this technique at Sandia, which are featured as examples.

---

## 1. Introduction

The early 1970's was a period rich in activity for the area of ion-beam analysis (IBA). Some selected examples include -- 1970: the pioneering work by Johansson et al. [1] in Particle Induced X-ray Emission (PIXE) spectrometry; 1972: invention of the nuclear microprobe by Cookson and Pilling [2]; 1972: first external-beam PIXE (X-PIXE) analysis (of liquids) by Deconninck [3]; 1974: another X-PIXE study by Jolly et al. [4]; culminating in 1975 with the first combination of nuclear microprobe and external-beam analysis (an apparent tie between Horowitz and Grodzins [5] and Cookson and Pilling [6]). Over the years this combination -- eXternal Micro Ion Beam Analysis (X-MIBA) -- has proven to be quite synergistic, spawning results and applications which would have been impossible to achieve through either technique by itself.

Virtually every type of IBA has now been performed using X-MIBA with the exception of channeling and Elastic Recoil Detection (ERD). External Nuclear Reaction Analysis (X-NRA) was demonstrated first in 1976 by Deconninck [7], and Rutherford Backscattering Spectrometry (X-RBS) depth profiling was initially performed in air by our group in 1983 [8]. Scanning Transmission Ion Microscopy (STIM) was first accomplished in air in 1987 by our group [9]. External-beam Nuclear Reaction Analysis (X-NRA) depth profiling of deuterium was first reported just last year (1989) by both our group [10] and by Laursen et al. [11]. When these IBA and microprobe techniques are performed externally, there are advantages and disadvantages which must be considered for a given analytical application. The potential advantages of X-MIBA are:

1. Any state of matter can be examined (solid, liquid, gas).
2. Sample size and shape not restricted.
3. Sample positioning simplified considerably.
4. Analysis throughput increased significantly.
5. Charge build-up eliminated.
6. Beam heating minimized.
7. Sample volatility caused by exposure to the vacuum or the beam reduced.
8. Beam energy easily scanned by adjusting window-target separation.
9. Handling of radioactive samples facilitated.
10. Regions of interest on large samples easily identified.
11. Computer-automated data acquisition can utilize existing hardware/software used for in-vacuum microprobe analysis.

Some of the disadvantages of X-MIBA include:

1. Spatial resolution degrades due to scattering in foil/air.
2. Beam-window/air interactions can decrease sensitivity by increasing background.
3. Energy straggling in window/air increases uncertainties in analyses.
4. Window-foil rupture can cost time/money.
5. Direct exposure to external beam can be fatal.
6. External beam can generate hazardous quantities of radioactive reaction products in the air and sample.
7. External beam interactions with the target ambient can modify the target at the analysis spot.

Many of these pros and cons of X-MIBA have been pointed out by Williams [12] in a recent review of external beam analyses and Lovenstran and Swietlicki [13] in a recent description of the new X-MIBA system at LUND. Deconninck [7,14] has also prepared reviews of non-vacuum analysis which are recommended. At the Sandia X-MIBA facility, we

have found that the advantages of: unrestricted sample size, simplified sample positioning and increased throughput have been the main benefits of applying this analysis technique in our fusion materials program. There have been numerous occasions when non-destructive analysis (e.g., one, two and even three dimensional concentration profiles) of large Tokamak components (such as entire limiters) required rapid turn-around so that these critical and expensive parts could be shipped back to the site for continued use. Further, we have found that all of the disadvantages listed above can either be circumvented through good experimental technique, or are more than offset by the substantial advantages afforded by in-air analysis.

We will review in this paper the current status of X-MIBA with emphasis on 1) present facilities, 2) radiation hazards, 3) analysis techniques, and 4) examples selected to demonstrate the unique and powerful multidimensional analysis capability of this emerging analytical technique. Evan Williams prepared a review of PIXE analysis with external beams in 1984 [12] which is highly recommended. This review also contained an excellent section on external milli/micro-probes, and should be thought of as a companion to this paper.

## 2. Facilities

At the present time, an increasing number of nuclear microprobe laboratories are implementing the option of operating with an external beam. It is interesting to note that the highest resolution (2-4 $\mu$m diameter) external microbeam work was also the earliest [6]. The X-MIBA method has clearly not been exploited for applications which require extremely high spatial resolution. In fact, most X-MIBA is performed with beams that have spot sizes of 100 $\mu$m or larger (so-called "millibeams"). These beams are about two orders of magnitude greater in diameter than the state-of-the-art beams used for in-vacuum nuclear microprobe applications. In general, the best results are obtained by performing nuclear microprobe analyses in a vacuum chamber, but X-MIBA becomes indispensable for those applications where the sample is not vacuum compatible. Table 1 lists some of the facilities which either 1) possess small external beam spots through the use of focusing or micro-collimation or 2) utilize relatively large millibeams but still obtain scanned elemental images of samples.

### 2.1 X-MIBA System Layout

A diagram of the X-MIBA system at Sandia in Albuquerque, NM, USA is shown in fig. 1. This system has been in operation for approximately 10 years and shares many of the characteristics of other external microprobes. In a typical experiment, an ion beam is extracted from an EN tandem Van de Graaff accelerator and transmitted to the external beam system via our nuclear microprobe beamline and optics. The final ion-optical element of the microprobe (the left-most component shown in fig. 1) is a small bore quadrupole-doublet lens (F. Martin type) which is used to focus the beam onto the center of a 1 mm diameter exit window. The beam passes through an in-vacuum annular Si surface barrier detector in its transit between the lens and the window. As will be described below, this detector is used both for X-RBS and as a monitor of beam intensity. Following passage through the foil, the beam is transmitted through air (or a controlled atmosphere of He in some systems) to the target which is mounted on an XY table controlled by stepping motors. Characteristic x-rays or gamma rays produced in the sample are detected by Si(Li) or Ge detectors (not shown in fig. 1) which are mounted in air, while charged particles resulting from scattering or nuclear reactions are detected with Si surface barrier detectors mounted either in air or back inside the vacuum system.

2.2 Windows

A rather extensive literature exists concerning the optimal selection of the material used for the exit foil for X-PIXE/PIGE [29,34-38], X-RBS [8,39] and X-NRA [11,16]. Some probes use tiny pinhole exit apertures instead of thin windows [26] which eliminates problems such as increased backgrounds and beam spreading due to beam-window interactions, but adds to the complexity of the system by requiring differential pumping. Nevertheless, the highest spatial resolution X-MIBA systems use either pinhole exit apertures or else mount the samples directly onto the exit window.

As can be determined from table 1, most X-MIBA systems use kapton (thickness 7.5$\mu$m) windows. Kapton is a polyimid plastic which is fairly resistant to radiation damage, and therefore, these windows survive exposure to MeV ion beams for considerably longer periods than other polymers such as mylar [39]. In general, for X-PIXE and X-PIGE applications, it is best to use an exit foil which does not contain elements which generate radiation which interferes with signals from the target sample.

While kapton is preferred for X-PIXE and X-PIGE, there are problems with the use of this material for some of the other external analysis techniques. For example, one way to perform X-RBS is with the detector in-vacuo (as shown in fig. 1), and for this geometry the scattering from the exit foil is observed. Scattering from a kapton window will interfere with signals from light elements in the sample (e.g. C, N, or O), but usually does not obstruct scattering from heavy elements (e.g. Fe-Au). On-the-other-hand, if a metal foil (e.g. stainless steel or Ni) is utilized, then the scattering from heavy elements in the sample are obscured while the signals from light elements are detected without interference. We therefore use a 5 $\mu$m stainless steel foil for our X-RBS profiling of C which is discussed in the next section. Rauhala et al. [39] perform X-RBS with the detectors in air, and therefore, are not sensitive to scattering from the exit foil. For this geometry, kapton was shown to be preferred based on both resolution and durability.

Lee et al. [16] have recently shown that extremely uniform and thin foils are required to minimize the propagation of experimental errors in the deconvolution of D($^3$He,p) yield vs. energy data to determine X-NRA depth profiles of D in samples. These errors (up to 20%) were shown to stem from energy broadening which was a result of transmission through foils of non-uniform thickness. While this effect can theoretically be taken into account [10], this is an unnecessary complication of the analysis. Electron-beam evaporated ultra thin windows composed of Al (0.92 $\mu$m) and Au (0.22 $\mu$m) were shown to survive irradiation and to cause an energy spread of less than 50 keV for $^3$He ions incident at 2.5 MeV.

Several X-MIBA laboratories are currently exploring the use of 0.5 $\mu$m $Si_3N_4$ films which are attached to Si reticules. These films are formed by depositing a thin layer of $Si_3N_4$ on a single crystal wafer of Si and then back-etching from the Si side. Such windows are currently used as ultra-thin windows for x-ray spectrometers, and initial results of their use as exit windows for X-MIBA applications look promising [40].

Ironically, the record for the thinnest exit foil was set very early in the history of PIXE. Seamen and Shane [41] brought a 3.0 MeV proton beam (30 nA) through a 0.13 $\mu$m Ni foil. While they suggested that the survivability of this foil was good for low beam currents, no one has tested this claim.

A discussion on exit windows would not be complete without addressing the problem of breakage and the resultant vacuum failure. Kapton foils seem to survive accumulated beam doses of from $10^{18}$-$10^{19}$ ions/cm$^2$, and metal foils tend to last even longer. It has been our experience, however, that window lifetime depends more on the attention of the operator than

on radiation damage. These thin windows are generally glued to an exit snout, such as the one shown in fig. 1. These windows easily rupture or become detached if a target sample accidentally comes in contact with the snout (especially during a lateral or vertical scan). While such accidents are just about unavoidable, there are precautions which can be taken to minimize the consequences of the loss of vacuum on both the beamline and accelerator system. Anttila et al. [29] developed an ingenious safety valve built into the extraction snout which automatically closes at the onset of a vacuum failure. Most systems rely on commercially available fast acting valves, but on the Sandia X-MIBA system, this valve protects only the accelerator.

The principle behind pin-hole extraction circumvents the problems associated with foil lifetime as well as improving the spatial resolution of the beam on target. Barfoot et al. [26] use a nozzle fabricated from graphite with a exit aperture of only 8 $\mu$m diameter. This small diameter permits maintenance of a pressure less than 0.1 Pa in the microprobe, and an upstream source aperture of 250 $\mu$m further isolates the microprobe from the accelerator system. The microprobe vacuum system is pumped by both TM and oil-diffusion pumps.

## 2.3 Focusing

Focusing adjustments on the Sandia X-MIBA system are made by viewing the luminescence of a removable glass slide mounted flush with the end of the exit nozzle (not shown in fig. 1). It is very important to use a slide with a thickness significantly greater than the range of the extracted beam to avoid exposure which, as discussed below, can result in severe radiation injuries. Thin microscope cover slides should therefore be avoided. The extraction snout is mounted onto an "acu-port" (see fig. 1) which facilitates the positioning of the 1mm exit foil to match the focal point of the quadrupole doublet lens.

Several groups have measured the lateral spatial distribution of the in-air beam as a function of air gap [5,13,16,26]. The results of such a measurement for an external $^3$He beam (initial ex-vacuo energy of 2.15 MeV) on the Sandia system [16], which for this experiment used the 1.14 $\mu$m Al/Au window, is shown in fig. 2. As can be seen from this figure, the main contribution to beam width is the angular distribution that the ion beam has as it emerges from the exit window foil and the subsequent distance of travel in air. A TRIM calculation suggests that the scattering in air of the $^3$He beam contributes only a negligible broadening to the $^3$He beam compared to broadening caused by the foil, and this explains the superior resolution obtained by pin-hole systems [26]. Lovestam and Swietlicki [13] measured that a 2 MeV proton beam broadened to only 200 $\mu$m upon passage through 1 cm of air; this is ~1/3 what we measured for the $^3$He beam (see fig. 2). Barfoot et al. [26] measured the broadening of a 3 MeV proton beam extracted through a pin hole to be only 24 $\mu$m in an air gap of 2.5 mm. These results suggest that the optimal lateral resolution of an external microbeam would be obtained by using a pin-hole system and where possible by minimizing the lateral straggling of the beam in air by utilizing a very high energy proton beam.

The experimental beam width data plotted in fig. 2 includes the contribution of the initial beam spot size on the foil which is ~100 $\mu$m. It is obvious that for air-gaps of several mm, that it is not necessary to obtain a finely focused spot at the exit foil. This allows operation of the microbeam with the micron slits relatively wide open, and results in significantly higher beam currents than are typically obtained for high lateral resolution applications of the nuclear microprobe.

## 2.4 Beam Current Monitoring/Normalization

All quantitative analysis experiments require accurate knowledge of the beam current delivered to the target. The reliability of X-PIXE and X-PIGE analyses was recently examined by Wookey and Rouse [42]. They found that measuring the current on an isolated exit snout shorted to the sample adequately determined the beam current. While there was incomplete charge collection arising from escaping electrons emitted by the foil, air and sample, they claim that this effect was small.

It is difficult to accurately measure the current this way for some samples (e.g. insulators, liquids or gases). For these samples other approaches which normalize the analysis have been used. Deconninck [7] used internal monitors in both standards and samples in the analysis of liquids. K X-rays from the monitor element (As) were detected and used to normalize the analysis. Recently, Laursen et al. [11] have used Zr K X-rays generated by Zircaloy samples to normalize X-NRA analyses of deuteride blisters which form on pressure tubes. Another approach is to normalize the data based on either X-rays or $\gamma$-rays produced when the beam passes through the exit window as done by Deconninck and Bodart [14]. Our group [10,16] has used the backscattering signal from the window itself (scattering from Au in an Au/Al couple) to normalize X-NRA of deuterium in fusion reactor components.

# 3. Radiation Hazards

The introduction of energetic ions into the atmosphere creates three potential radiation hazards. The most obvious danger is direct exposure to the external beam. The irradiation rates caused by exposure to the direct beam are, as we will demonstrate, extremely high, and pose a very serious health hazard. Exposure to ions scattered from external targets (or created by nuclear reactions in the targets) is also a potential danger. The third hazard of external ion beam operation arises from the radionuclides produced via the interaction of the energetic ions with the atoms of the atmosphere.

The degree of potential danger created by an external ion beam experiment depends upon many variables. Ion species and energy, beam size and current, target composition, physical configuration of the experiment and, perhaps most importantly, experimental procedures, are all factors which influence the radiation safety of external beam experiments. The Sandia external ion beam facility is most frequently used for two types of analyses, X-PIXE using up to 4.5MeV $H^+$ ions, and X-NRA using 3.1MeV $^3He^+$ ions. We present here a brief description of the methods and results of calculations done to estimate the hazards of performing these analyses using the experimental arrangement shown in fig. 1.

## 3.1 Direct Beam Dose Rates

Direct exposure to the external ion beam clearly presents the greatest danger to the operator. Simple, easily followed procedures should be established to ensure that no one is ever exposed directly to the external beam. The consequences of accidental exposure to the direct beam can be calculated (in terms of radiation exposure rate, R) by

$$R = I_i \, E_{ion} \, 1/V \, 1/\rho \, C_{rad} \, rbe. \qquad (3.1)$$

$I_i$ is the ion beam current, $E_{ion}$ is the ion energy, V is the volume of skin affected (beam area x penetration depth of the ions in skin), $\rho$ is the density of skin, $C_{rad}$ is the energy to radiation absorbed dose conversion factor, and rbe is the rad to rem (radiation equivalent man, 100rem=1Sv) conversion factor [43]. R is the dose rate equivalent in rem/s. The dose rate equivalent delivered by a 1nA beam of 4.5MeV $H^+$ (3.1MeV $^3He^+$) ions at a distance in air

approximately 0.5cm from the exit window is 1.5 x $10^7$ (2.3 x $10^7$ rem/s). These values are many orders of magnitude above any recommended occupational radiation exposure rates. If however, the ion range in skin (~300 $\mu$m for 4.5Mev $H^+$, 50 $\mu$m for 3.1MeV $^3He^+$) does not exceed the depth of the epidermis or dead skin layer (which varies from ~50 to ~500 $\mu$m) then little or no irradiation damage will be inflicted. Penetration through the epidermis or irradiation of an open wound could have dire consequences, possibly including amputation following cell death and/or cancer growth [13]. Clearly direct exposure to an energetic external ion beam is to be avoided!

3.2 Scattered Beam Dose Rates

Another safety concern during the operation of the external beam is radiation from ions backscattered from the targets or radiation created by nuclear reactions in the target. Calculations have been performed to quantify these exposures at various distances from the target in the backscattering hemisphere. This calculation of the exposure rates by backscattered external ion beams assumes the following: (1) the targets are placed at the minimum range from the exit window (0.3cm for X-NRA or 1cm for X-PIXE), (2) the initial backscattered energy is equal to the initial in-vacuum beam energy (i.e., the target is massive and negligible energy loss occurs in the exit window) and postscattering energy loss in air is accounted for, but the depth range of ions in the skin is considered to be constant at the maximum value, and (4) the incident beam current is 1nA. The external beams of interest were again 3MeV $^3He^+$ and 4.5MeV $H^+$.

Equivalent dose rates due to backscattered energetic ions were determined in a manner similar to that used for direct exposure. Equivalent dose rates were determined with the equation

$$R_b = \Phi_b \, E_{bion} \, 1/V \, 1/\rho \, C_{rad} \, 1/A \text{ rbe.} \tag{3.2}$$

$\Phi_b$ is the backscattered ion flux, $E_{bion}$ is the backscattered ion energy in ergs, V is the volume of skin affected, $\rho$ is the density of skin, $C_{rad}$ is the energy to radiation absorbed dose conversion, A is the area exposed, rbe is the rad to rem conversion factor and $R_b$ is the exposure rate to backscattered ions in rem/cm$^2$•s [43].

A similar equivalent dose rate calculation has also been made for the secondary charged particles emitted during X-NRA analysis of deuterium using the D($^3$He,p) reaction. The protons produced by this reaction have an energy of about 14MeV and to first approximation can be assumed to be distributed isotropically. They create an equivalent dose rate $R_p$ given by:

$$R_p = \Phi_p \, K, \text{ where} \tag{3.3}$$

$$K = E_p \, 1/V \, 1/\rho \, C_{rad} \, 1/A \text{ rbe, and} \tag{3.4}$$

$$\Phi_p = \sigma_p \, \Omega \, Nt_d. \tag{3.5}$$

$E_p$ is the energy of the proton when it reaches the skin, $\sigma_p$ is the D($^3$He,p) reaction cross section as a function of the incident $^3He^+$ energy, $\Omega$ is the solid angle for a given distance from the charged particle source that exposes 1cm$^2$ of skin, $Nt_d$ is the areal density of deuterium in the target, and V, $\rho$, $C_{rad}$, A, are as defined previously.

Figures 3a and 3b show contour plots of the calculated backscattered particle equivalent dose rates (in rem/cm$^2$•s) with respect to distance from the target beam spot for 1nA, 4.5Mev $H^+$ and 3.1MeV $^3He^+$ beams. The dose rates from the 14 MeV protons produced by X-NRA

of a target containing an areal density of 2 x $10^{18}$ D/cm$^2$ were added to the dose rates calculated for the backscattered $^3He^+$ ions to produce a total equivalent dose rate in the backscattered direction for external D($^3$He,p) nuclear reaction analysis. (The dose rates from the $^4$He particles also produced by the reaction are negligible compared to the backscattered $^3$He and thus were not included in the figure). Figure 3 demonstrates that care should be taken to avoid exposure to the backscattered beam. For example, the exposure of a sizable portion of the face to the D($^3$He,p) nuclear reaction backscattered radiation can result in doses of 1 rem in a matter of seconds, even at distances up to a meter away from the target.

A point to consider about exposure to typical external ion beams is that normal radiation monitoring techniques such as neutron monitors, gamma detectors and personal film badges, do not effectively record ion irradiation doses. A priori establishment of safe experimental procedures is an excellent idea for external ion beam work.

### 3.3 Radionuclide Production Rates

The nuclear reaction of external beam ions with the atomic constituents of the atmosphere create the third hazard of external beam work - atmospheric radionuclides. Atmospheric radionuclides create exposure problems both externally and internally (if inhaled into the lungs). The hazard posed by radionuclide production was determined for the 1nA 4.5MeV $H^+$ and 3.1MeV $^3He^+$ ion beams considered above. The rate of radionuclide production $\alpha$, was calculated to a first approximation in the following manner:

$$\alpha = I \sigma C r. \tag{3.6}$$

I is the ion beam current (#/s), $\sigma$ is the reaction cross section (cm$^2$), C is the target atom concentration (#/cm$^3$), r is the range (cm) in air for which the ion retains an energy greater than $Q_m$ of the reaction. The reaction cross-sections were obtained from various sources in the literature [44]. The cross section used in each calculation was taken to be the mean of the extremes of the cross sections for that reaction in the energy region of interest. The cross section was then considered to be constant with respect to ion energy from the maximum energy down to $Q_m$ of the reaction. The production rates for radionuclides in air by X-PIXE and X-NRA under the conditions detailed in section 3.2 are presented in table 2. These radionuclide production rates were instrumental in determining the maximum values for energy and beam current used on Sandia's external beam system. The values in table 2 correspond to derived air concentrations of radionuclides (DAC) in our facility about an order of magnitude less than those requiring special air monitors and filtering as established by the United States Department of Energy (DOE) [45]. (The DAC depends upon variables such as room volume, ventilation, etc, and thus is highly facility-specific.) Higher energies and beam currents would push the Sandia facility over the acceptable DAC limits set by the DOE.

It is a simple fact that external ion beams present potential radiation hazards. These hazards may prove difficult to monitor but can be largely eliminated with simple precautions such as shielding, limiting access to the target area, and providing special ventilation as needed.

## 4. X-MIBA Analytical Techniques and MFE Examples

In this section we will describe several techniques used for X-MIBA. These techniques will be elucidated by examples selected from our own application of this tool primarily in the area of Magnetic Fusion Energy (MFE) research. More specifically, the study of the aftermath of the plasma-wall interaction with in-vessel components such as limiters or divertor plates using X-MIBA techniques will be discussed. It should be pointed out that the X-MIBA

technique has been widely applied to many scientific areas including: 1) geology, 2) biology and medicine, 3) archeometry, and 4) materials science [12] in addition to MFE research.

The use of X-MIBA has been an important tool in gaining an understanding of the complex transport of both fuel (H-isotopes) and impurities which occurs in the edge-region of magnetically confined high-power plasmas. As indicated above, the main advantages of external analyses in the case of MFE applications have been unrestricted sample size, ease of positioning/scanning and rapid turn-around. In addition, the X-NRA analysis developed for deuterium [10,11] is the only technique currently available which can be used for nondestructive studies of this type [46,47]. Knowledge of deuterium content in first-wall components is central to an accurate prediction of tritium retention in the walls of reactors such as the Tokamak Fusion Test Reactor (TFTR) or the Joint European Torus (JET) which will both attempt DT fusion experiments later this decade. Since starting our X-MIBA studies of MFE wall components in 1983, over 300 parts from over a dozen different MFE reactors have been examined (points, 1D, 2D and even 3D concentration profiles have been carried out. Finally, since one of the objectives of this paper is to describe the microscopic application of X-MIBA, MFE examples have been selected which showcase the multidimensional elemental imaging capabilities of these techniques.

4.1 Data Analysis

In the case of X-PIXE, X-PIGE and (usually) X-NRA, one detects a signal (i.e. an x-ray, $\gamma$-ray or an energetic charged particle) which is characteristic of the element being analyzed; however, as opposed to X-RBS which will be discussed below, this signal carries very little direct information concerning the depth distribution of the element under investigation. To perform quantitative measurements with these techniques a thick-target yield analysis is performed to obtain a relationship between signal intensity and the concentration. The approach taken for in-vacuum PIXE is well described in a recent book by Johansson and Campbell [48] and virtually no modification, except taking air absorption into account, is required to apply these techniques to ex-vacuo applications.

In the case of X-RBS, the energy of the detected signal contains both target-mass and depth information, which, in principle, can be sorted to yield a concentration depth profile. The standard analysis of this type of data has been discussed in several books including one edited by Mayer and Rimini [49]. To make this treatment applicable to the ex-vacuo geometry, the scattering and energy loss of the beam in air and in the exit foil must be considered. For simple targets, e.g. thin layers of heavy elements on light substrates, it is in principle easy to convert raw X-RBS data into a 3D concentration profile, but to our knowledge, this has been done only for in-vacuum RBS applications of nuclear microprobe analysis [15].

A large number of points are examined during imaging applications of X-MIBA. For example, a 64x64 pixel scan results in the examination of 4096 separate points, and if 128x128 pixels are used, this number increases to 16,384. It is clear that short-cuts and approximations must be used to analyze this data to obtain quantitative information; performing this many thick-target yield analyses or RBS simulations would require far too much time and effort. In addition, the statistics of data used for imaging usually does not warrant such a rigorous analysis.

Data analysis considerations are considerably simplified if a thin target approximation is valid. In this case, thin target standards are commonly used to quantify X-MIBA experiments, and are of particular value for determining the areal densities of elements which are restricted to the very near surface of the sample. The usual equation used to relate the areal density of an unknown to that of a standard is:

$$N = N_{st} (Y/Y_{st}) \quad , \tag{4.1}$$

where Y and $Y_{st}$ are the yield of counts from the sample and standard, respectively, normalized to the incident number of beam projectiles used during the analysis, and N and $N_{st}$ are the areal densities of the element examined in the sample and standard, respectively. This equation is accurate if the cross-section of the nuclear or atomic process used to produce the detected signal remains relatively constant in both the sample and the standard, if target matrix effects (e.g. absorption) are negligible, and if sample and standard analysis geometries are the same.

Under special circumstances, the thin target approximation (expressed in eq. (4.1)) can also be used to determine the areal density of elements thick targets. We define an "apparent" areal density, $N'(E_o)$, for an incident energy of $E_o$ by:

$$N'(E_o) = (1/\sigma_o) \int c(x)\, \sigma[E(x)]\, dx \quad , \tag{4.2}$$

where $\sigma_o$ and $\sigma[E(x)]$ are the reaction cross sections at the surface and at depth x (beam energy = E(x) ), respectively, and c(x) is the concentration depth profile. In equation (4.2), the measurement of the "apparent" areal density $N(E_o)$ assumes that the thin target yield equation given in (4.1) applies (which of course it doesn't in this case, hence the term "apparent"). The integration range in (4.2) extends over the range of the incident projectile. If c(x) can be characterized by p parameters, then measurements of N' at p different energies, $\{E_o\}$, will uniquely determine c(x) and thereby yield the true areal density. This analysis requires that both the cross sections and stopping powers are known. An example of such a determination of thick target areal density will be given below where a two-parameter model is used for c(x), and simple analytical equations result which are compatible with the rapid quantification required for elemental-mapping applications.

4.2 X-PIXE

The earliest practitioners [5,6] of external nuclear microbeam analysis utilized PIXE more than any other ion-beam analytical technique, and this is still true today. Some recent examples which involve the creation of composition-based images by X-PIXE include the deciphering of ancient documents by Lovestram and Swietlicki [13] and the mapping of elements found in cataracts by Koyama-Ito et al. [33].

In fig. 4 we show an X-PIXE example selected from one of our MFE applications [50,51]. This figure displays a 3D rendering of the amount of Fe deposited on the surface of the ALT-I pumped limiter, from two different perspectives. This limiter was designed to pump the plasma of the TEXTOR tokamak located in Julich, FRG. X-MIBA was the only technique capable of providing this information because of the large size of this limiter, 30x30x8 cm, and the desire to reuse this expensive component in TEXTOR at a later date. The scattering geometry is shown in fig. 1. A 4.5 MeV proton beam was used (~4.2 MeV on target), and X-PIXE data was collected over a 64x64 grid covering the limiter front face in addition to several line scans along the sides. The x-ray intensities were converted to elemental areal densities through the use of standards and eq. (4.1), and the information from nearly 5000 data points was mapped onto a computer generated 3D model of the ALT-I limiter (shown in fig. 4)

The shape of the limiter is fairly easy to discern: the front face (30x30 cm) has the shape of a saddle, and the plasma makes contact (as defined by the last closed magnetic flux surface) at the center of this face; from the ion side view (an EMF is induced in a Tokamak plasma loop which tends to drive positive ions one way and electrons the other) one can see the throat

(a black strip) through which the plasma is pumped; there is not a similar throat on the electron side.

This limiter was fabricated out of graphite and coated with ~20 $\mu$m of TiC. All of the Fe which is observed therefore resulted from plasma discharges in TEXTOR. Seven other elements were monitored along with Fe, and an analysis of the composition of the layer indicated that it was similar to that of stainless steel. This data suggested that the source of this impurity layer was stainless steel main limiters in TEXTOR which are eroded by the plasma. Such investigative uses of X-PIXE are now common and have great value in identifying impurity generation sources in tokamaks in addition to screening components for unintentional contamination prior to their use.

The Fe deposition pattern displayed in fig. 4 was accurately reproduced by theoretical models [51] (not shown in the figure). These analyses together with the theoretical models have provided considerable insight into impurity transport in the tokamak edge and have proven to be extremely valuable for the design of future limiters and divertor systems.

4.3 X-RBS

While there are considerably fewer examples of X-RBS as compared to X-PIXE in the literature, for those applications which exist, X-RBS was the only technique capable of providing the required data. The nondestructive measurement of coating thickness (up to 50 $\mu$m) is a good example of such a unique use of X-RBS. X-PIXE cannot be as easily used for layers of this thickness due to attenuation in the target.

As mentioned above, the two scattering geometries used for X-RBS have the detector either outside [39] or inside the vacuum chamber [8]. In fig. 5 we plot X-RBS spectra for external 4.5 MeV proton scattering using the latter geometry (see fig. 1) for graphite (top) or TiC coated graphite (bottom two) samples. The TiC coated samples were typical of those used for the ALT-I limiter described above. The salient features of the RBS spectra include the scattering from the 5 $\mu$m stainless steel exit window (labeled SS) the N and O peaks resulting from the ~1 mm of air path between the foil and the sample, the C edge just below N, and the irregular (non-Rutherford) scattering signal from Ti (not labeled--the region between 2.5-3.7 MeV).

Measurement of the coating thickness was accomplished converting the energy scale (lower abscissa) to a C depth scale (upper abscissa) by calculating the energy loss in the TiC sample, air path, and exit foil. The thickness could then be determined by the inflection point in the C signal (near 1.4 MeV) which reflects the change in the sample material from TiC (~50% C) to graphite (100% C). The two TiC coated samples labeled A and B were of slightly different thicknesses, and these tests indicated that the coating TiC coating thickness could be determined absolutely within 1.0 $\mu$m, and relative thickness changes could be determined with an accuracy of .2$\mu$m.

X-RBS measurements performed prior to and after the use of the ALT-I limiter shown in fig. 4 showed no TiC thickness change in the center region of the 30x30 cm face while erosion of levels approaching one micron were observed near the lower right-hand corner (and presumably near the other corners as well) due to erosion. The TiC coating on the sides was found to increase slightly in thickness, which was explained by redeposition of TiC eroded from the corners of the face.

### 4.4 X-NRA

Several charged particle nuclear reactions have been suggested and demonstrated for use in external ion beam analyses but few have actually been used. Deconninck [7] first demonstrated X-NRA by showing that the $^{14}N(d,\alpha)$ reaction could be used to externally detect N. We showed that the $^{14}N(\alpha,p)$ reaction could also be used to detect N using an external 10 MeV $\alpha$ beam [8]. Raisanen [52] and our group [8] have shown that the highly exothermic $^{7}Li(\alpha,p)$ reaction is very well suited to externally depth profile Li in samples. Two groups have used the $D(^{3}He,p)$ reaction to detect [11] or profile [10,16] deuterium with external $^{3}He$ beams.

Our applications of X-NRA mapping of deuterium have been applied, usually in conjunction with X-PIXE, to address the codeposition of deuterium, carbon and other impurities onto tiles and components in a number of tokamaks around the world. The primary emphasis, however, has been focused on the TFTR facility located at the Princeton Plasma Physics Laboratory. One of the driving concerns at TFTR is that the small amount of tritium (T), only 5 gms, which will be allowed on the PPPL site will quickly become buried in the tokamak first walls and thereby jeopardize the demonstration of controlled thermonuclear fusion breakeven using DT plasmas. Our D-mapping efforts have been aimed at determining the total amount of D retained in the wall components of TFTR, with updates of the measurements being periodically made upon each opening of the device. So far extensive D-mapping has been accomplished two times, once in 1987 and again in 1988. A third set of wall samples was received during the preparation of this paper. Most of our studies have involved the analysis of a selected subset of the ?2000? inner-bumper graphite limiter tiles which make up nearly 20 $m^2$ of the internal area of TFTR.

#### 4.4.1 Thin Targets

A D-map on one of these tiles is shown in fig. 6, together with a photograph of the tile. This analysis was performed using a fixed energy 750 keV on-target beam combined with a two-dimensional lateral scan. The proton yields from the $D(^{3}He,p)$ reaction were measured with the external detectors shown in fig. 1, and were converted to areal densities using a standard and the thin-target yield equation given in (4.1). The tile was sampled at 64x64 points across its plasma-facing surface. The upper two-thirds of this tile was severely ablated by multi-MeV runaway electrons generated within TFTR. Comparison of the photographic and D-images in this figure shows clear regions of correlation between the surface morphology and the D-content over the surface of the tile.

Contrary to what one might expect, the most severely ablated regions contain the most D. This has lead us to believe that because material is lost from this area, the resultant recessed region is shadowed from the constant plasma-scouring which takes place in adjacent regions. D thereby builds up in these ablated regions. Subsequent analyses have shown that a considerable amount of D accumulates on the sides of the tiles used in TFTR because these regions are also protected from the edge plasma. The accumulation of D in such recessed areas is not negligible, and measurements indicate that such areas will account for almost 1/4 of the tritium inventory in TFTR.

#### 4.4.2 Thick Targets

A principle challenge when applying X-MIBA for elemental-imaging of samples which require thick target yield analyses is that of identifying ways to simplify or approximate the computations. As indicated above, such analyses usually involve data of low statistics which rarely warrant rigorous computations (i.e. numerical integration, nonlinear least-square fitting, etc.)

Such an approximation has been developed for the analysis of deuterium areal densities and deuterated layer thickness for deposits on tokamak limiter and divertor tiles. It was found using the standard in-vacuum D($^3$He,p) depth profiling technique that the D concentration profiles for similar components usually decayed exponentially in depth [47,10]

$$c(x) = c_o \exp(-x/\mu) \quad , \tag{4.3}$$

where $c_o$ is the D concentration at the surface of the tile, and $\mu$ is the characteristic e-folding length. The "true" areal density of a profile given by equation (4.3) is $N_{true} = c_o\mu$.

The apparent areal densities (eq. (4.2)) for an exponential D profile in graphite were numerically calculated for several values of incident energy $E_o$ as a a function of $\mu$, and are plotted, normalized to $N_{true}$, for incident $^3$He energies of 750 and 1800 keV in fig. 7. These apparent areal densities are also determined experimentally using thin deuteride standards and applying eq. (4.1). It is clear that the average of these two apparent areal densities (also plotted in fig. 7) provides a reasonably accurate (within 20%) determination of the true areal density for values of $\mu$ less than 4 $\mu$m. It is conceptually quite easy to understand why this averaging approach works so well. For D profiles which decay rapidly from the surface (i.e., $\mu$ < .4 $\mu$m), both the 750 and 1800 keV measurements yield the same apparent density which equal the true areal density. For D profiles which decay slowly from the surface (i.e., 0.4 $\mu$m < $\mu$ < 4 $\mu$m), the 750 (1800) keV measurement underestimates (overestimates) the true areal density, but the average of these two measurements is quite accurate. The two inserts in fig. 7 are meant to illustrate this effect for a profile which has a flat-top shape. For values of $\mu$ greater than 4 $\mu$m, the approximation breaks down. Experimental determination of $\mu$ can also be obtained through the ratio of the apparent areal densities. Nonlinear least-square curve fits were used to arrive at the following relationship:

$$\mu = 1.006\,[N'(1800)/N'(750)-1]^{1/2} + 0.00134\,[N'(1800)/N'(750)-1]^{9/2} \quad , \tag{4.4}$$

which is also reasonably accurate up to $\mu$ = 4 $\mu$m. It is trivial to obtain both the areal density and characteristic depth, $\mu$, from the raw data because the approximations are analytical.

The results of a thick target analysis is shown in fig. 8. For this experiment the target sample was an undamaged mid-plane tile removed from the bumper limiter of TFTR following the 1988 run campaign. The interesting D-deposition pattern in this case is caused by the plasma-shadowing effect of adjacent tiles and is not damage as was the case for fig. 6.

Measurements of this kind have been performed on other tiles from TFTR [46]. The combination of this data with similar analyses of points near tile and wall coupon centers is allowing the first experimental determinations of global D retention in large thermonuclear fusion reactors. Our results on TFTR indicate that for the fueling scenarios planned for DT fusion breakeven experiments, that ~ 2 gm of T will accumulate on the plasma-faces of the bumper limiter tiles, 1 gm of T will be retained on the sides of these tiles, and another 1 gm of T will be deposited on the remainder of the vessel wall. The total of 4 gm T which we predict will be retained is close to the 5 gm limit which is allowed on the PPPL site.

## 5. Conclusions

In this review of eXternal Micro Ion Beam Analysis (X-MIBA) we have tried to update the current status of this important micro-analytical technique. The capabilities afforded by in-air elemental analysis of targets of any state of matter, size, and shape are benefits unique to this powerful technique. It is clear, however, that X-MIBA is not exploited fully because,

until recently, only a small fraction of nuclear microprobe facilities have had an external-beam capability. This fraction is increasing, however, as more and more scientists recognize the advantages of X-MIBA.

Table 1. Facilities which perform X-MIBA.

| Lab | ion/E MeV | Diameter $\mu$m | Window | Ref. |
|---|---|---|---|---|
| USA | | | | |
| Sandia-Albuquerque | H/4.5 | 40-1000 | SS,Be | 15 |
| | $^3$He/3 | | Au/Al | 10,16 |
| Sandia-Livermore | H/10 | 25 | SiN | 17 |
| Los Alamos | H/3 | 1000 | kapton | 18 |
| Bartol, U. Del | H/1.2,2 | 50-500 | kapton | 19 |
| Brookhaven | H/2.5 | 5 | none | 20 |
| Brooklyn, CUNY | H/2.5 | 20 | kapton | 21 |
| Davis, UC | H/4.1 | 1000 | kapton | 22 |
| Lincoln Lab. | H/2 | 25 | none | 23 |
| Cornell | H/3 | <1000 | kapton | 24 |
| U. of Oregon | ? | ? | ? | 25 |
| Canada | | | | |
| Queens U. | H/3 | 10 | none | 26 |
| | $^3$He/1.3 | 30 | Ni | 11 |
| European Comm. | | | | |
| LARN, Namur | H/3 | 700 | Al | 27 |
| La Louvre, Paris | H/4 | 1000 | | 28 |
| Helsinki | H/2.5 | >1000 | kapton | 29 |
| LUND | H/2.5 | 400 | kapton | 13,30 |
| Harwell | H/2.9 | 4 | kapton | 31 |
| Asia | | | | |
| Fudan U., Shanghai | H/1.5-3 | 40 | kapton | 32 |
| IMS, U. of Tokyo | He/27 | 100 | kapton | 33 |

| X-PIXE | | X-NRA | |
|---|---|---|---|
| nuclide | rate (#/s) | nuclide | rate (#/s) |
| C11 | 3.84E+06 | O15 | 1.20E+07 |
| O15 | 1.53E+06 | F18 | 5.47E+06 |
| F18 | 4.34E+05 | N13 | 5.08E+05 |
| F17 | 5.26E+04 | C11 | 1.27E+04 |
| N13 | 6.89E+01 | O14 | 4.33E+02 |
| Total | 5.86E+06 | Total | 1.80E+07 |

table 2, Production Rates of Radionuclides by External Beams

Figure Captions

1. Experimental apparatus for eXternal Micro Ion Beam Analysis (X-MIBA) at Sandia National Laboratories, Albuquerque.

2. Experimental and deduced contributions to external-beam ($^3$He) spatial width as a function of transmission length in air.

3. Contour plots of equivalent dose rates (rem/cm$^2$•s) versus distance from the target beam spot due to (a) backscattered $H^+$ from a 4.5MeV, 1nA beam, and (b) the combination of backscattered $^3He^+$ from a 3.1MeV, 1nA beam and the 14MeV $H^+$ reaction products of the D($^3$He,p)$^4$He reaction on a D areal density of 2 x $10^{18}$ /cm$^2$.

4. Surface areal densities of Fe contamination on the ALT-I TiC coated graphite limiter after 2000 discharges in TEXTOR. Note that the artificial color scale to the right is in units of $10^{15}$ atoms/cm$^2$.

5. Linear plot of X-RBS of C reference (top), as received TiC/C (bottom) and ion eroded TiC/C (middle) with 4.5 MeV protons and a stainless steel exit window. The spectra are offset for clarity.

6. (a) A 64x64 pixel artificial color map of deuterium deposited on the plasma facing surface of a damaged bumper limiter tile removed from TFTR following the 1987 campaign and (b) a photograph of the same tile showing the correspondence between surface morphology and D-deposition.

7. Theoretical calculations of the "apparent" to "true" D-areal density ratio using equation (4.2) and an exponential concentration profile given in equation (4.3) as a function of the characteristic e-folding length, $\mu$, for the D($^3$He,p) nuclear reaction analysis. The three curves are calculated for incident 750 and 1800 keV $^3$He and their average. When this ratio is unity, the measured areal density using thin target analysis assumptions is accurate.

8. Thick target analysis of D-areal density (lower) and D-profile characteristic e-folding length (thickness) of the deposit on a tile removed from the mid-plane of the inner bumper limiter of TFTR. The areal density map was determined by averaging the apparent areal densities resulting from D($^3$He,p) analysis with incident 750 and 1800 keV $^3$He, while the thickness plot was determined through the ratio of these yields and applying equation (4.4).

**References**

* Work performed at Sandia National Laboratories supported by U.S. Department of Energy under contract DE-AC04-76DP00789.

1. T. B. Johansson, R. Adelsson and S. A. E. Johansson, Nuclear Instruments and Methods 84 (1970) 141.

2. J. A. Cookson and F. D. Pilling, AERE Report R6300 (1972).

3. G. Deconninck, Journal of Radioanalytical Chemistry, 12 (1972) 162.

4. R. K. Jolly, G. Randers-Pehrson, S. K. Gupta, D. C. Buckle and H. Aceto, Proc. Third Conf. on Applications of Small Accelerators, Denton, Texas, 1974, NTIS Report CONF741040-PI.

5. P. Horowitz and L. Grodzins, Science 189, 795 (1975).

6. J. A. Cookson and F. D. Pilling, Phys. Med. Biol., 20 (1975) 1015.

7. G. Deconninck, IEEE Publication 76CH 1175-9 NPS, (1976) 533.

8. B. L. Doyle, Nuclear Instruments and Methods 218 (1983) 20.

9. B. L. Doyle, unpublished data.

10. S. R. Lee and B. L. Doyle, Nuclear Instruments and Methods B40/41 (1989) 823.

11. T. Laursen, M. Leger, Xin-Pei Ma, J. d. MacArthur, G. R. Palmer and J. L. Whitton, J. Nuclear Materials 165 (1989) 156.

12. E. T. Williams, Nuclear Instruments and Methods B3 (1984) 211.

13. N. E. Göran Lövestam and E. Swietlicki, Nuclear Instruments and Methods B43 (1989) 104.

14. G. Deconninck and F. Bodart, Nuclear Instruments and Methods 149 (1978) 609.

15. B. L. Doyle, J. Vac. Sci. Technol. A3 (3), May/June 1985.

16. S. R. Lee, D. S. Walsh and B. L. Doyle, Nuclear Instruments and Methods B45 (1990) 281.

17. A. E. Pontau, Private communication.

18. J. R. Tesmer, C. J. Maggiore and D. M. Parkin, Nuclear Instruments and Methods B40/41 (1989) 718.

19. C. P. Swann, Nuclear Instruments and Methods B22 (1987) 407.

20. R. E. Shroy, H. W. Kraner, K. W. Jones, Nuclear Instruments and Methods 157 (1978) 163.

21. E. T. Williams, G. C. Noel, A. Guardala, M. Salasruiz and J. A. Chamberlain, Jr., Nuclear Instruments and Methods B40/41 (1989) 624.

22. R. A. Eldred, B. H. Kusko and T. A. Cahill, Nuclear Instruments and Methods B3 (1984) 579.

23. M. Aronson and P. Horowitz, Nuclear Instruments and Methods 180 (1981) 125.

24. J. W. Mayer, private communication.

25. U of Oregon stuff.

26. K. M. Barfoot, J. D. Macarthur and C.Vargas-Aburto, Nuclear Instruments and Methods 197 (1982) 121.

27. G. Deconninck, G. Demortier and F. Bodart, Atomic Energy Review Suppl. No. 2 (1981) 151.

28. T. A. Cahill, private communication.

29. A. Anttila, J.Raîsänen and R. Lappalainen, Nuclear Instruments and Methods B12 (1985) 245.

30. K. G. Malmqvist, L. Asking, H.-C Hansson, R. Hellborg, G. Hylten, E.-M Johansson, S. A. E. Johansson, P. Kristiansson, P. Larsson, N.E. G. Lövestam, B. G. Martinsson, J. Pallon, B. Svantesson, E. Swietlicki, U. A. S. Tapper and K. Thermner, Nuclear Instruments and Methods B40/41 (1989) 685.

31. J. A. Cookson and F. D. Pilling, Phys. Med. Biol. 21 (1976) 965.

32. Jian-Xin Chen, Hong-Kou Li, Chi-Gang Ren, Guo-Hun Tang, Xi-De Wang, Fu-Chia Yang and Hui-Ying Yao, Nuclear Instruments and Methods 168 (1980) 437-440.

33. Hiroko Koyama-ito, Eiko Wada, Toru Tsumita, Masato Horiuchi and Shuzo Iwata, Nuclear Instruments and Methods B3 (1984) 625.

34. B. Raith, H. R. Wilde, M. Roth, A. Stratmann and B. Gonsior, Nuclear Instruments and Methods 168 (1980) 251.

35. J. Räisänen and A. Anttila, Nuclear Instruments and Methods 196 (1982) 489.

36. R. Raith, A. Stratmeann, H. R. Wilde, B. Gonsior, S. Brüggerhoff and E. Jackwerth, Nuclear Instruments and Methods 181 (1981) 199.

37. A. Katsanos and A. Hadjiantoniou, Nuclear Instruments and Methods 149 (1978) 469.

38. J. Räisänen, Nuclear Instruments and Methods ??????? 638.

39. E. Rauhala, J. Räisänen, and M. Luomajärvi, Nuclear Instruments and Methods in Physics Research B6 (1985) 543.

40. A. E. Pontau, private communication.

41. G. G. Seaman and K. C. Shane, Nuclear Instruments and Methods 126 (1975) 473.

42. C. W. Wookey and J. L. Rouse, Nuclear Instruments and Methods in Physics Research B18 (1987) 303.

43. C. S. Bushong, "Radiologic Science for Technologists, Physics, Biology and Protection 3rd e. (C. V. Mosby co., 1984) Chapter 1.

44. F. K. McGowan and W. T. Milner, Atomic and Nuclear Data Reprints Volume 2, Charged Particle Reaction List 1948-1971 (Academic Press, New York, 1973), ed., K. Way.

45. Radiation Protection for Occupational Workers, Department of Energy Order 5480.11 (December 1988).

46. D. S. Walsh, J. M. Knox and B. L. Doyle, Nuclear Instruments and Methods in Physics Research B45 (1990), 62.

47. W. R. Wampler, B. L. Doyle, S. R. Lee, A. E. Pontau, B. E. Mills, R. A. Causey, D. Buchenauer, H. F. Dylla, M. A. Ulrickson and P. H. LaMarche, J. Vac. Sci. Technol. A6 (3) May/June 1988.

48. S. A. E. Johansson and J. L. Campbell, PIXE - a Novel Technique for Elemental Analysis (Wiley, 1988).

49. Ion Beam Handbook for Materials Analysis, edited by J. W. Mayer and E. Rimini (Academic, New York, 1971).

50. B. L. Doyle, R. T. McGrath and A. E. Pontau, Nuclear Instruments and Methods in Physics Research B22 (1987), 34.

51. R. T. McGrath, B. L. Doyle, J. N. Brooks, A. E. Pontau and G. J. Thomas, Journal of Nuclear Materials 145-147 (1987), 660.

52. J. Räisänen and R. Lappalainen, Nuclear Instruments and Methods in Physics Research B15 (1986) 546.

# X-NRA, X-RBS and X-PIXE using the Sandia Nuclear Microprobe

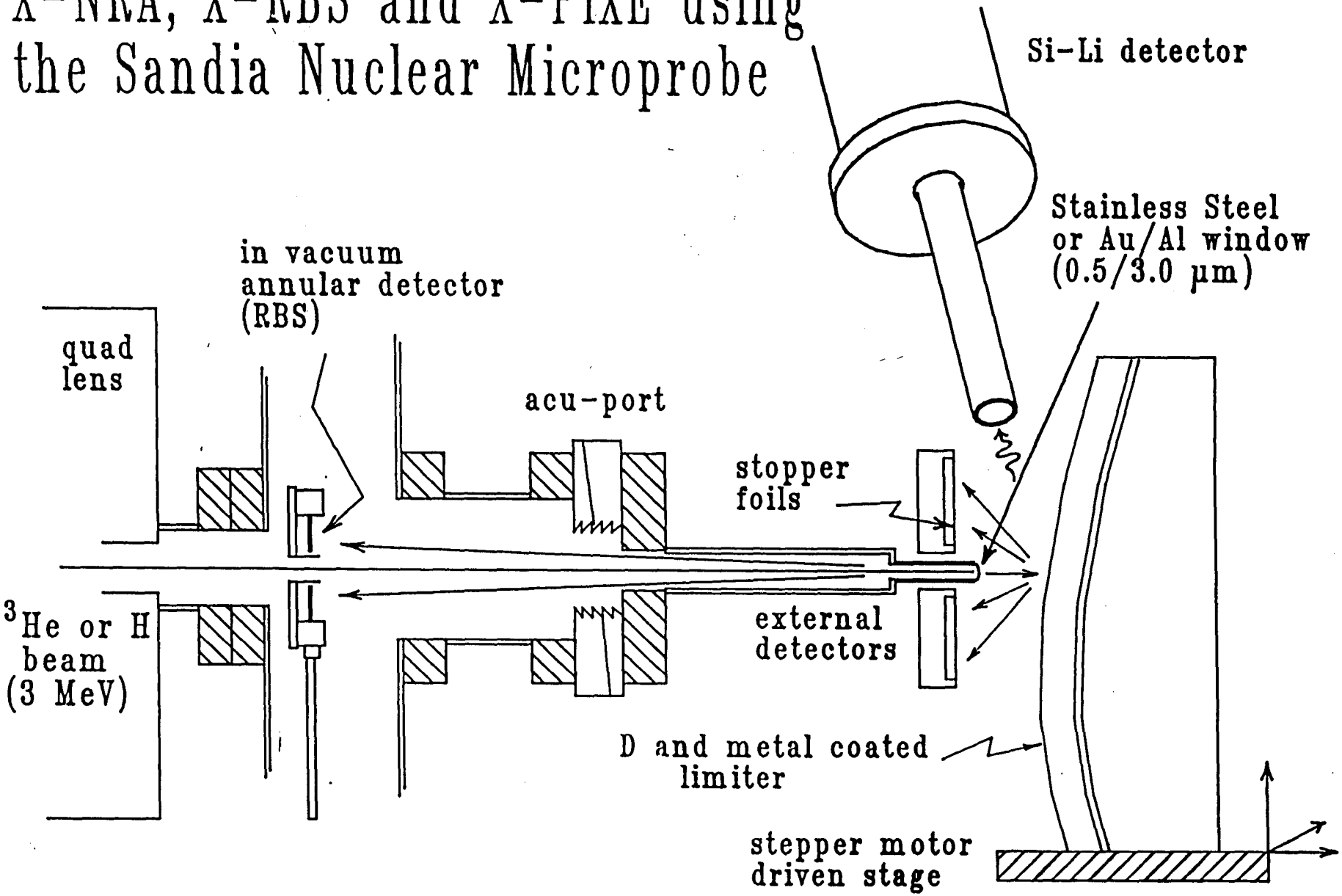


Figure 1

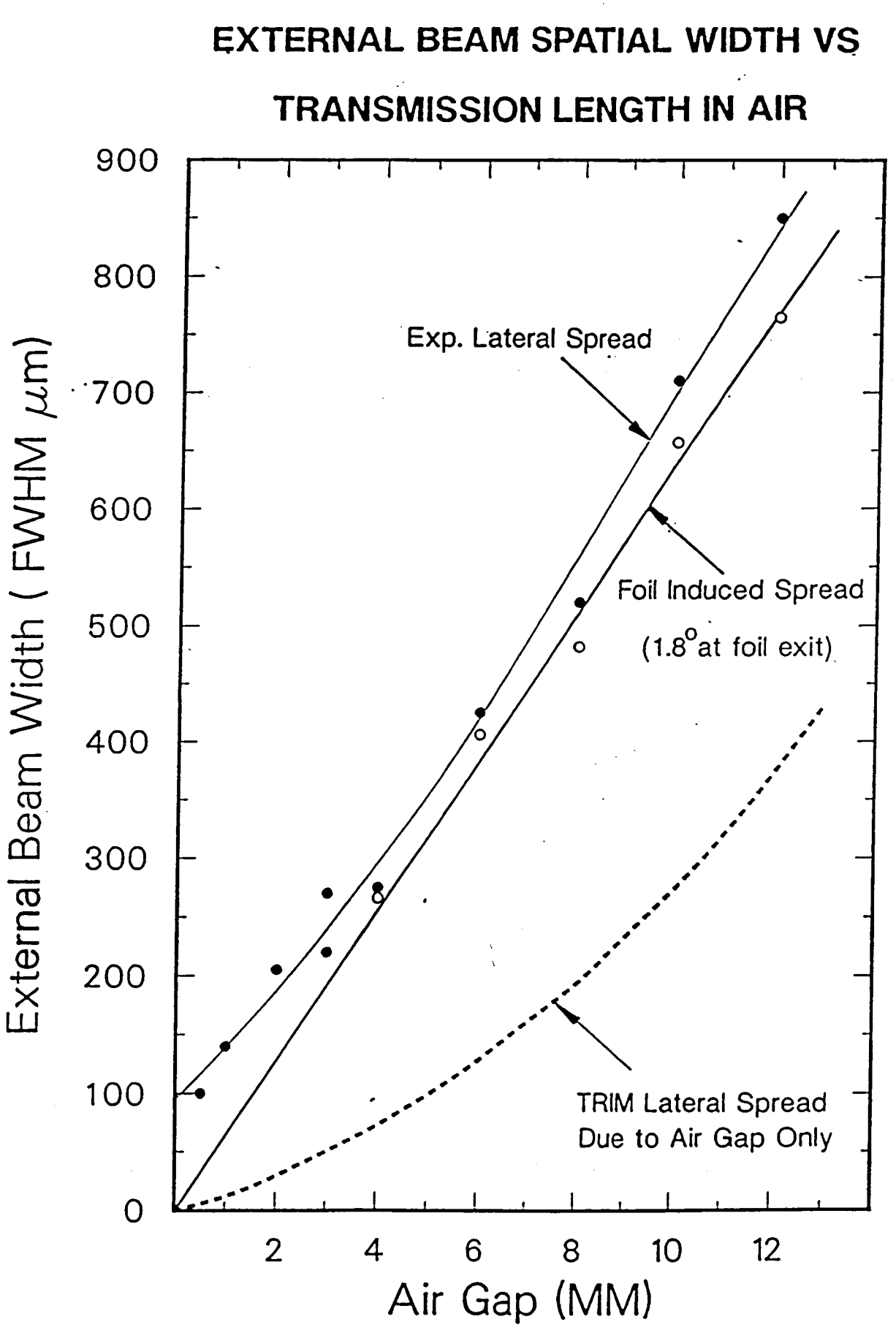
EXTERNAL BEAM SPATIAL WIDTH VS
TRANSMISSION LENGTH IN AIR
External Beam Width ( FWHM μm)
900
800
700
600
500
400
300
200
100
0
2
4
6
8
10
12
Air Gap (MM)
Exp. Lateral Spread
Foil Induced Spread
(1.8° at foil exit)
TRIM Lateral Spread
Due to Air Gap Only

Figure 2

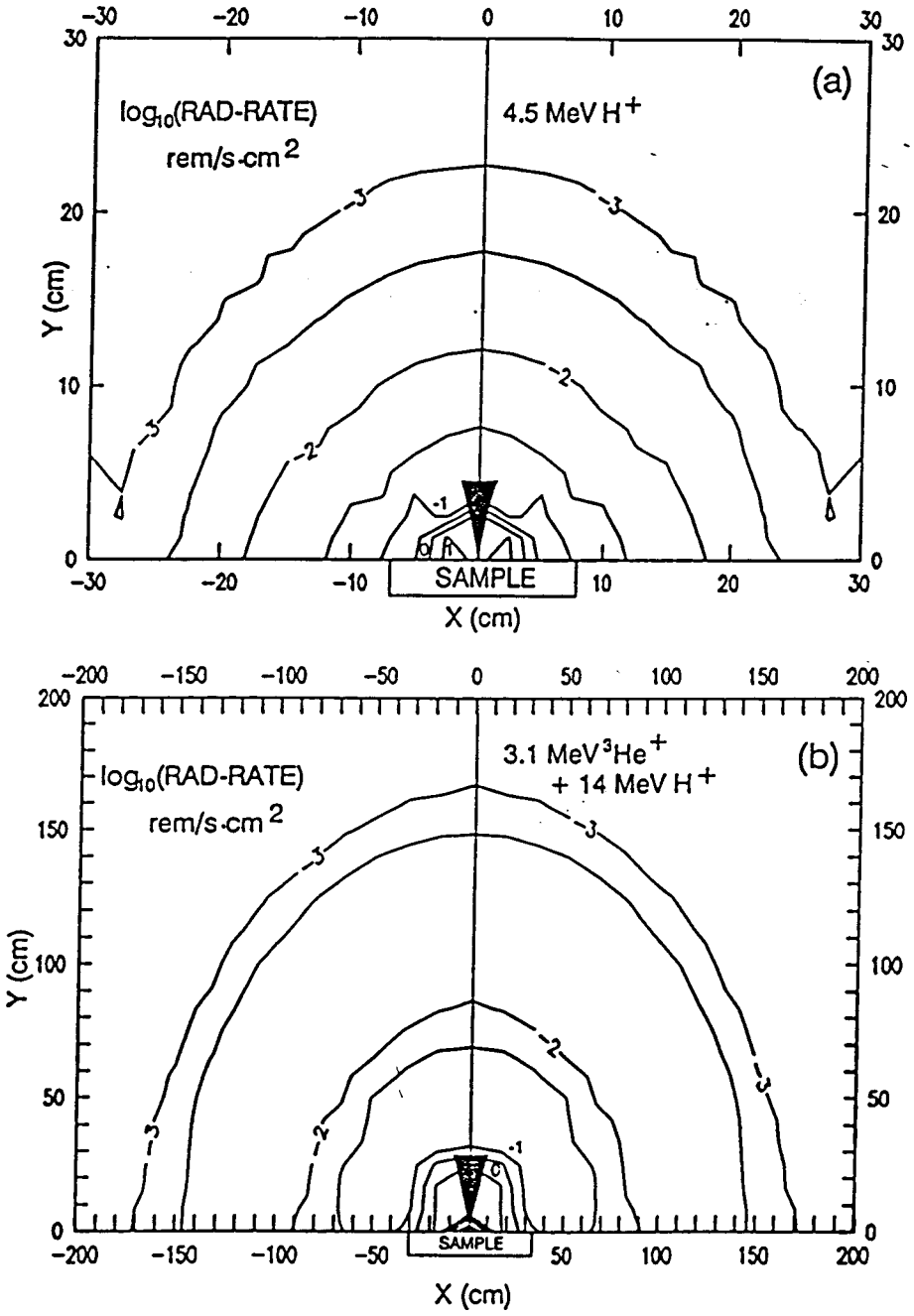
(a)
log10(RAD-RATE)
rem/s-cm2
4.5 MeV H+
Y (cm)
X (cm)
SAMPLE
(b)
log10(RAD-RATE)
rem/s-cm2
3.1 MeV 3He+
+ 14 MeV H+
Y (cm)
X (cm)
SAMPLE

Figure 3

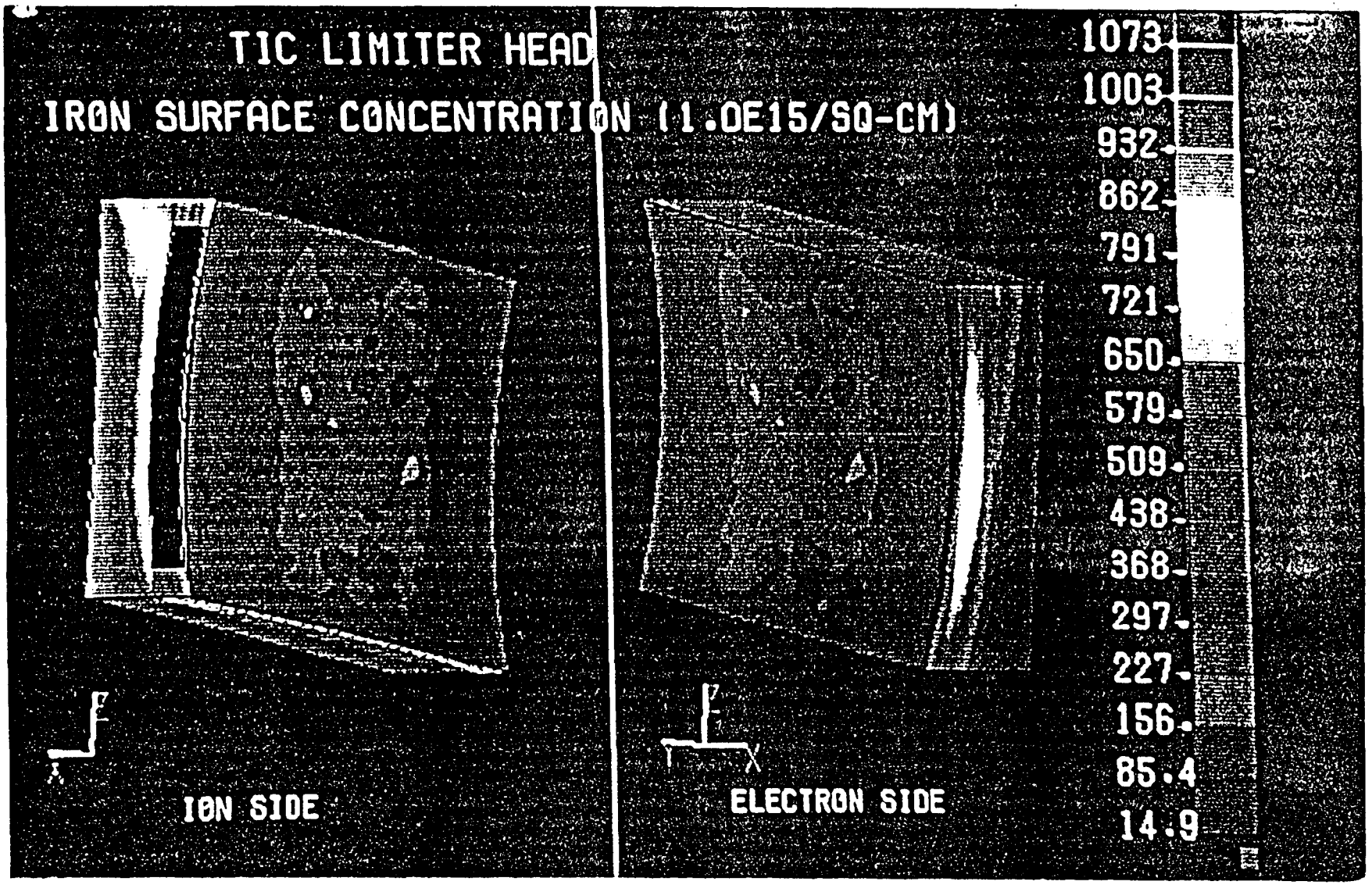
TIC LIMITER HEAD
IRON SURFACE CONCENTRATION (1.0E15/SQ-CM)
1073
1003
932
862
791
721
650
579
509
438
368
297
227
156
85.4
14.9
ION SIDE
ELECTRON SIDE

Figure 4

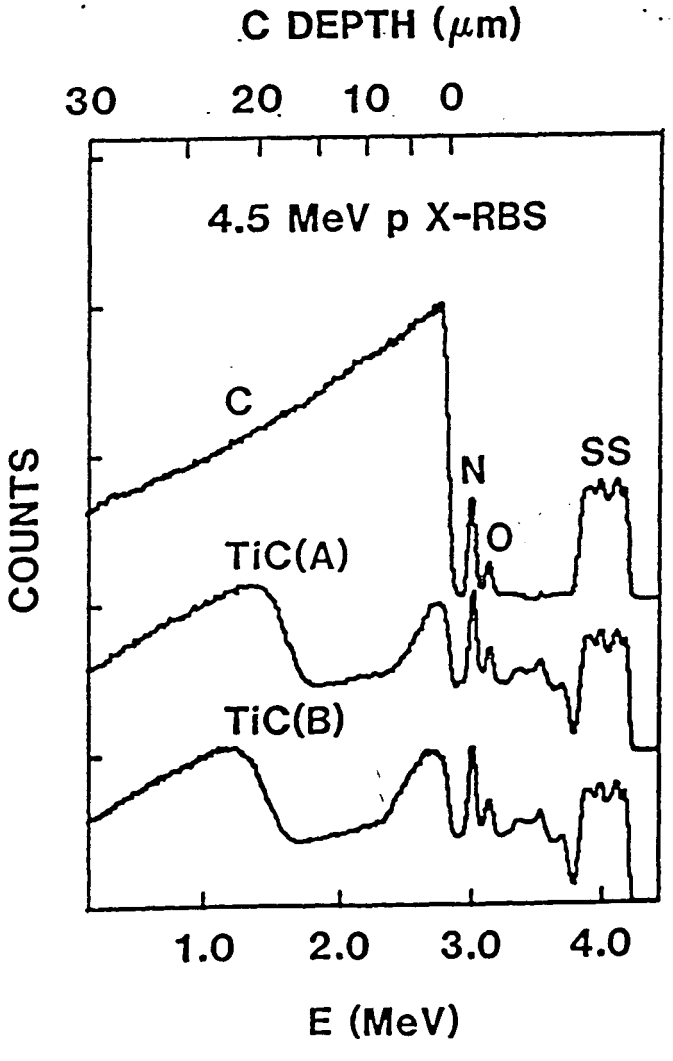
C DEPTH (μm)
30
20
10
0
4.5 MeV p X-RBS
C
N
SS
O
TiC(A)
TiC(B)
COUNTS
1.0
2.0
3.0
4.0
E (MeV)

Figure 5

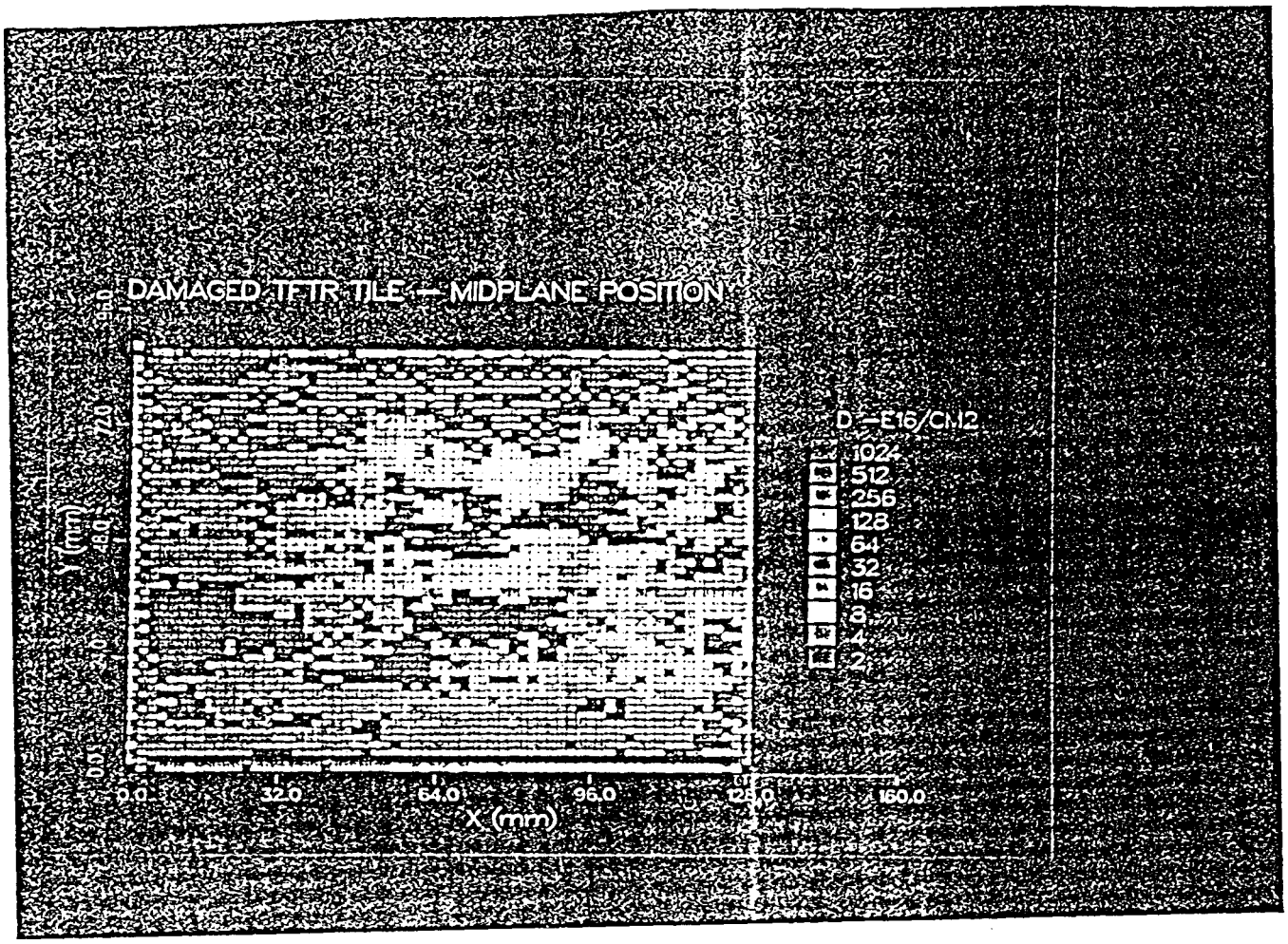


Figure 6a

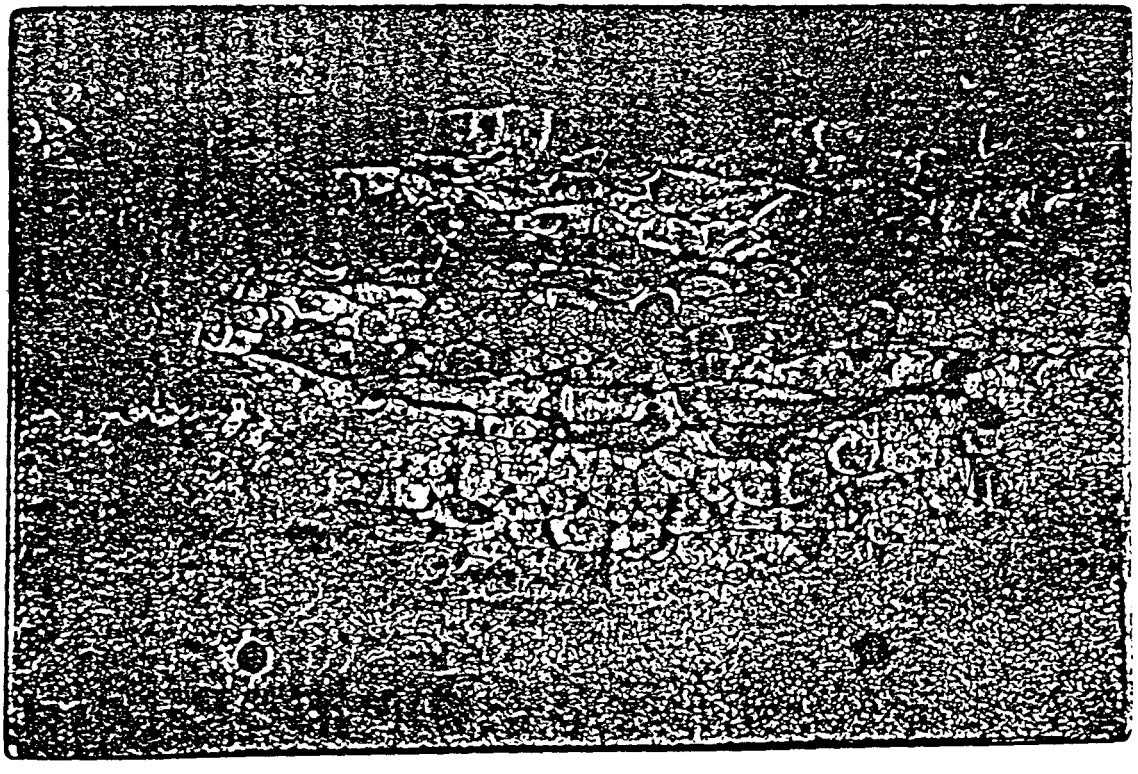

Figure 6b

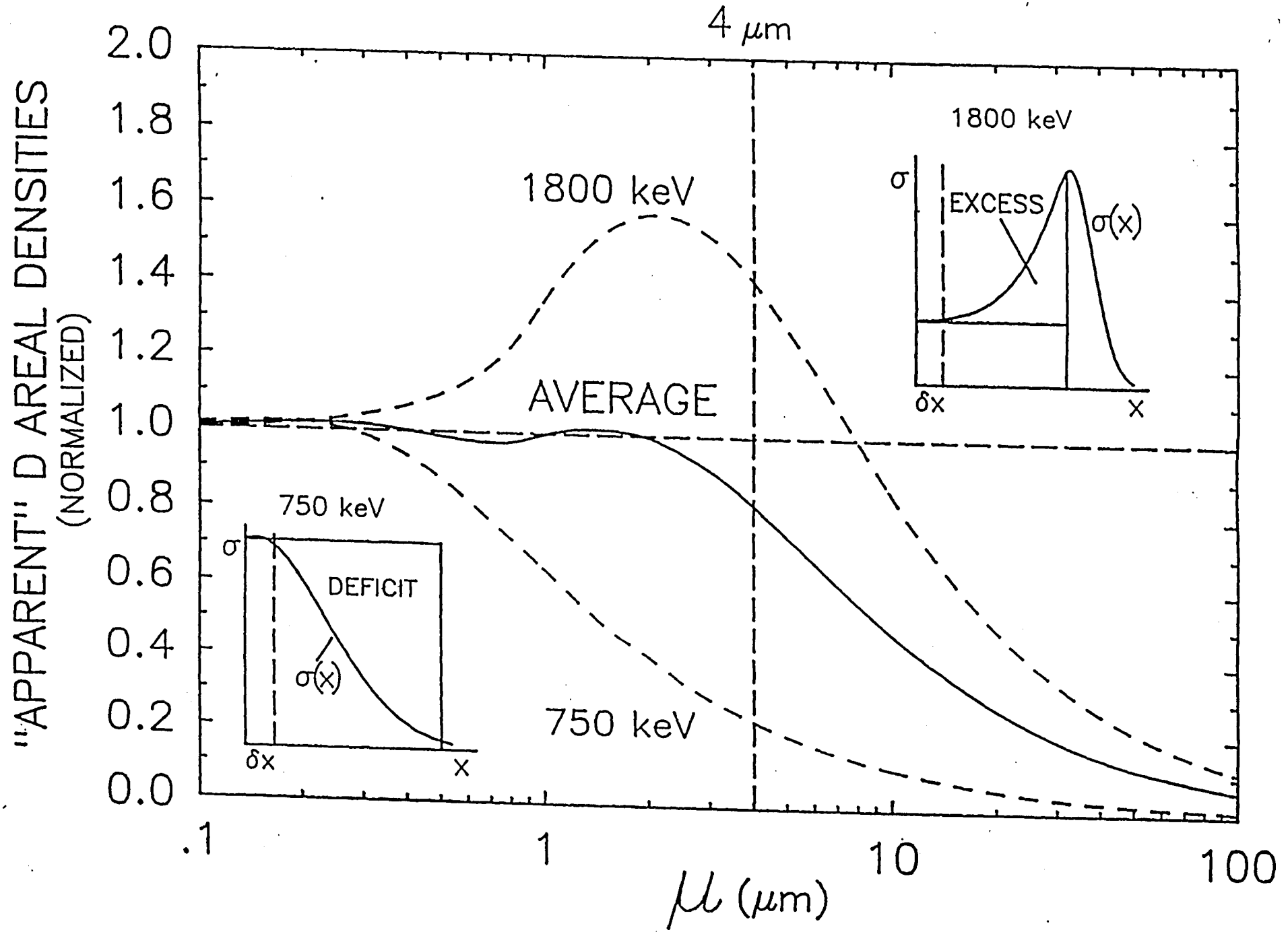
4 μm
"APPARENT" D AREAL DENSITIES
(NORMALIZED)
2.0
1.8
1.6
1.4
1.2
1.0
0.8
0.6
0.4
0.2
0.0
1800 keV
AVERAGE
750 keV
1800 keV
σ
EXCESS
σ(x)
δx
X
750 keV
σ
DEFICIT
σ(x)
δx
X
.1
1
10
100
μ (μm)

Figure 7

# THICK TARGET ANALYSIS OF D IN TFTR TILE #12

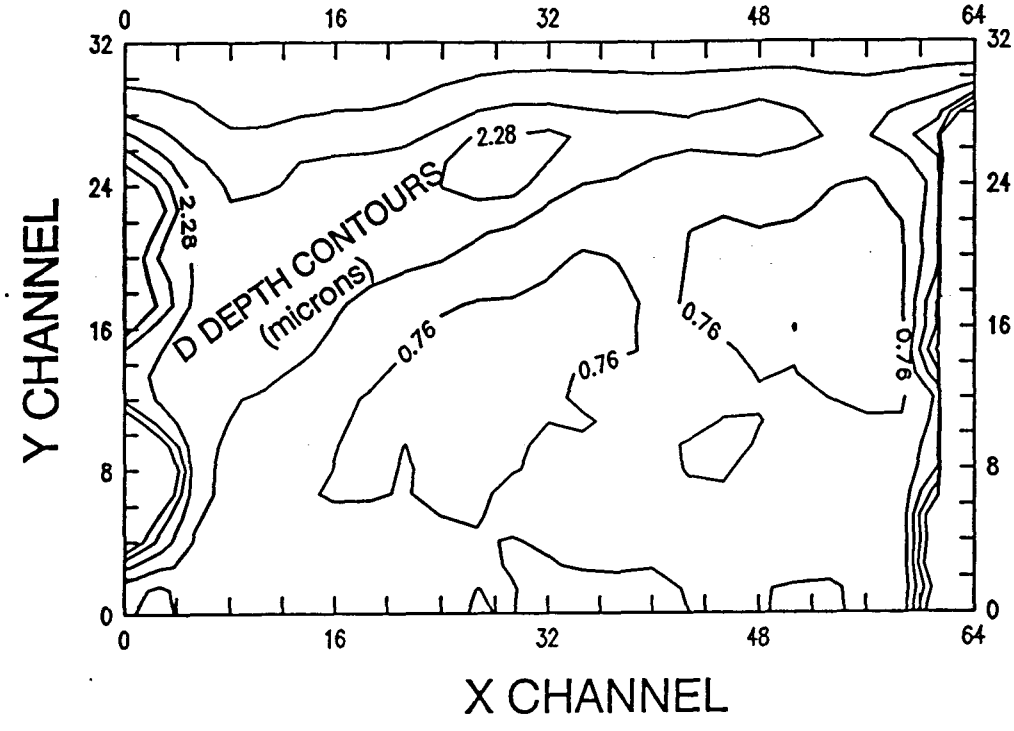


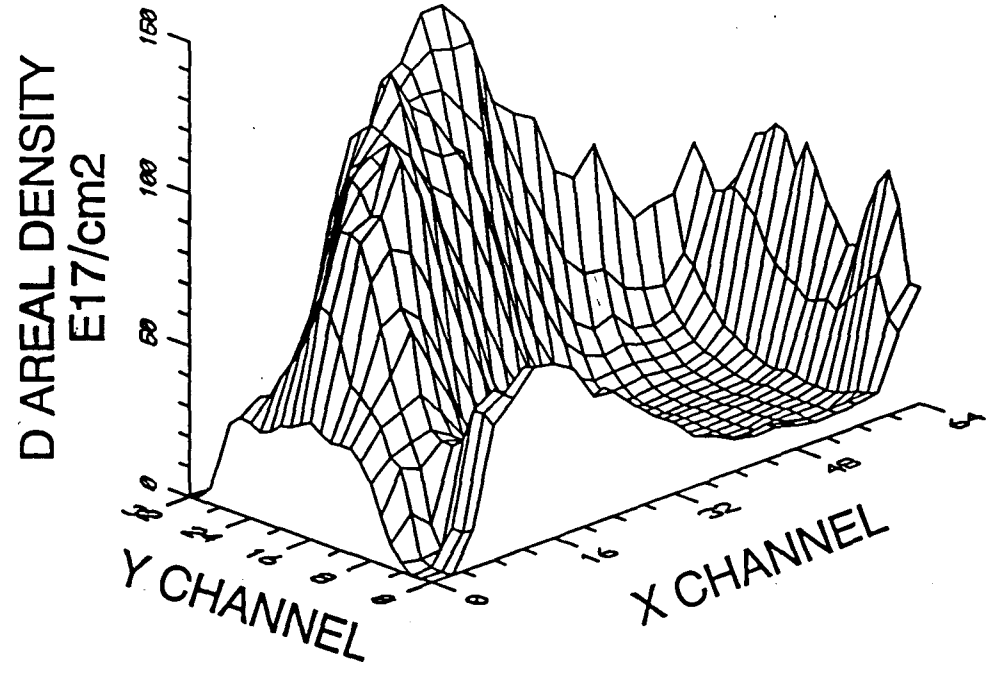


Figure 8